

Multiframe image estimation for coded aperture snapshot spectral imagers

David Kittle, Kerkil Choi, Ashwin Wagadarikar, and David J. Brady*

Fitzpatrick Institute for Photonics and Department of Electrical and Computer Engineering,
Duke University, 129 Hudson Hall, Durham, North Carolina 27708, USA

*Corresponding author: dbrady@duke.edu

Received 3 August 2010; revised 22 October 2010; accepted 30 October 2010;
posted 2 November 2010 (Doc. ID 132656); published 13 December 2010

A coded aperture snapshot spectral imager (CASSI) estimates the three-dimensional spatio-spectral data cube from a snapshot two-dimensional coded projection, assuming that the scene is spatially and spectrally sparse. For less spectrally sparse scenes, we show that the use of multiple nondegenerate snapshots can make data cube recovery less ill-posed, yielding improved spatial and spectral reconstruction fidelity. Additionally, data acquisition can be easily scaled to meet the time/resolution requirements of the scene with little modification or extension of the original CASSI hardware. A multiframe reconstruction of a $640 \times 480 \times 53$ voxel datacube with 450–650 nm white-light illumination of a scene reveals substantial improvement in the reconstruction fidelity, with limited increase in acquisition and reconstruction time. © 2010 Optical Society of America

OCIS codes: 110.4155, 110.4190, 110.4234, 120.6200.

1. Introduction

Coded aperture spectroscopy decouples spectral resolution and spectral throughput, enabling simultaneously large étendue and spectral resolving power [1–3]. Coded aperture designs may also be applied in push-broom geometries to capture full spectral images [4].

This architecture has been further extended by our group to develop a snapshot spectral imager using the spatial encoding from the coded aperture rather than push-brooming [5,6]. This instrument has been shown to effectively capture data at video rate from nonstationary scenes [6] and from beads in fluorescent microscopy [7]. The entire three-dimensional (3D) data cube is captured in a snapshot using a two-dimensional (2D) detector, where, unlike computed tomographic imaging spectrometers (CTISs) [8–10], the number of pixels in each channel of the data cube is equal to the total pixels of the detector. This yields an underdetermined system operator, specifying how much spatial or spectral detail can

be captured from a single snapshot. However, the efficiency of capture far exceeds noncompressive methods of snapshot spectral imaging, include the image mapping spectrometer (IMS) [11] and Lyot filtering [12], where these systems, like CTIS, require very large detector arrays.

Compressive spectral imaging (CSI) enables a reduction in the number of measurements needed to sample a full 3D data cube, exploiting the inherent sparsity of typical scenes. CSI leverages the emerging theory of compressive sensing (CS). CS states that sampling (significantly) below the Nyquist rate may be sufficient for accurate signal recovery if the product of the system measurement matrix and a sparsity transformation satisfies a certain sufficient condition called the restricted isometry property (RIP) [13]. The condition is difficult to verify in practice since such verification poses a nondeterministic polynomial-time hard (NP-hard) problem. Thus, the number of necessary measurements is often quantified by a quantity called incoherence, setting a sufficient condition for the RIP.

We now propose a new design of the coded aperture snapshot spectral imager by designing a 2D

push-broom variant, providing a multiscale estimation capability of the data cube. By taking additional snapshots of the same scene with codings that are distinct for each snapshot, it is possible to select the number of measurements based on resolution requirements while still maintaining the snapshot advantages of the instrument in each unique measurement. This provides flexibility in strictly adhering to the sparsity requirements needed for accurate estimation with compressive sensing. Additional examples of this method are found in [14,15].

This paper will follow with a discussion of the linear system model for multiple snapshots and a description of the algorithm used for reconstructing the data sets. In Section 3, changes to the physical instrument are outlined and, finally, the experimental results are presented comparing snapshot to multiframe reconstructions.

2. Theory

A. Computational Forward Model

The continuous model for power spectral density through the mask, prism, and optics at the detector is defined as [6]

$$f_{\ell}(x, y, \lambda) = \iint T_{\ell}(x', y') f_0(x', y', \lambda) h(x' - \phi(\lambda) - x, y' - y, \lambda) dx' dy', \quad (1)$$

where $T_{\ell}(x', y')$ is the transmission function representing the coded aperture for a particular snapshot encoding of the scene, $h(x' - \phi(\lambda) - x, y' - y, \lambda)$ is defined as the optical impulse response of the system, and $f_0(x', y', \lambda)$ is the power spectral density at the aperture code. The dispersion in the x direction is signified by $\phi(\lambda)$.

The discrete model of the intensity at each detector pixel (n, m) for the ℓ th single snapshot is given by [6]

$$g_{\ell, n, m} = \int_{\Lambda} \iint \iint T_{\ell}(x', y') f_0(x', y', \lambda) h(x' - \phi(\lambda), x, y', y, \lambda), \quad (2)$$

$$\text{rect}\left(\frac{x}{\Delta} - m, \frac{y}{\Delta} - n\right) dx' dy' dx dy d\lambda. \quad (3)$$

Assuming linear dispersion of the prism such that $\phi(\lambda) = \alpha\lambda$ and substitution of variables, along with the discretization of $T_{\ell}(x', y') = \sum_i \sum_n t_{\ell, i, n} \text{rect}(\frac{x'}{\Delta} - i, \frac{y'}{\Delta} - n)$, the discrete sampled data cube can be expressed as

$$f_{i, n, m} = \int_{\Lambda} \iint \iint \overbrace{\text{rect}\left(\frac{x''}{\Delta}, \frac{y''}{\Delta}\right)}^{\text{Detector}} \overbrace{\text{rect}\left(\frac{x'''}{\Delta}, \frac{y'''}{\Delta}\right)}^{\text{Coded Aperture}} \times f_0\left(x'' + i\Delta, y'' + n\Delta, \lambda' + \frac{m\Delta}{\alpha}\right) \times h\left(x'' - x''' - \alpha\lambda', y'' - y''', \lambda' + \frac{m\Delta - i\Delta}{\alpha}\right) \times dx'' dy'' dx''' dy''' d\lambda', \quad (4)$$

where (i, j) designate columns and rows of the mask, and (x, y) denote the spatial coordinates at the detector.

Finally, noting that $m + i = k$ and $i = k - m$, the detector measurements can be written as

$$g_{\ell, n, m} = \sum_i t_{\ell, i, n} f_{i, n, m+i} = \sum_k t_{\ell, k-m, n} f_{k-m, n, k}, \quad (5)$$

where $t_{k-m, n}$ is specified by the aperture code. Since the aperture code is shifted by a discrete amount $\Delta\ell$, specified by the size of a pixel mapped to the aperture code, the complete motion is a multiple of a for horizontal and d for vertical of $\Delta\ell$. The aperture code then models the transmission as $t_{\ell, i, n} = t_{i-a\Delta\ell, n-d\Delta\ell}$. This states that the final detector measurement is a projection of elementwise multiplication of the shifted aperture code with the scene. This can be algebraically expressed as a linear matrix system:

$$g_{\ell} = \Phi_{\ell} f. \quad (6)$$

Where Φ is a nonnegative mapping from the 3D voxels of the data cube f to the 2D detector array data, g_{ℓ} .

B. Extending the System Model

To extend the forward model for a snapshot measurement, let g_{ℓ} and Φ_{ℓ} denote the ℓ th snapshot CASSI measurement and its associated system forward model. Each g_{ℓ} is unique from chosen translations of the mask relative to the detector, yielding spectrally distinct coding and thus augmenting independent measurements. Since the mask moves relative to the detector, the uniqueness of each measurement g_{ℓ} is independent of the spatial diversity of the scene and additional g_{ℓ} augment the information of f if Φ_{ℓ} are independent. The forward model then becomes

$$g_{n, m, \ell} = \sum_i t_{i, n, \ell} f_{i, n, m, \ell, i}. \quad (7)$$

In matrix form, as in Eq. (6), this can be written as

$$\begin{bmatrix} g_1 \\ g_2 \\ \vdots \\ g_N \end{bmatrix} = \begin{bmatrix} \Phi_1 \\ \Phi_2 \\ \vdots \\ \Phi_N \end{bmatrix} f. \quad (8)$$

Since each g_ℓ is substantially smaller than f for multiple spectral channels, this system is highly underdetermined and, thus, cannot be solved by conventional inversion methods or least squares. Alternatively, theory from CS allows solving such underdetermined systems via sparsity-constrained optimization.

Compressive sampling, as opposed to Nyquist sampling, states that a signal can be accurately captured with fewer samples than that of the original signal [13]. In a traditional monochrome detector, the number of samples exactly matches the image, assuming there is no spatial correlation between pixels, which would be invalid for most natural scenes. When images are represented in a sparsifying basis, only a small number of coefficients are sufficient to accurately describe the image, yielding high compression. CS leverages this in the physical sensing stage rather than in the postprocessing stages, as is conventionally done. By extending this theory to spectral imaging, where a scene is sparse both spatially and spectrally, it is possible to compressively sample the 3D scene on a single detector.

The compressibility of the data cube depends on the sparsifying and measurement basis similarity, quantified by mutual coherence in Eq. (9):

$$\mu := \sqrt{N} \max_{i,j} |\langle \phi_i, \psi_j \rangle|, \quad (9)$$

where N is the length of the sequence to be measured, ϕ is the basis measurement, and ψ is the sparsifying basis. A lower value of μ indicates lower coherence (or *better incoherence*) between the measurement matrix and the sparsifying basis.

Lower mutual coherence requires fewer measurements for achieving a certain accuracy of the estimate (or solution). The compressibility of the system is scene dependent, reducing the flexibility of a compressive spectral imager unless tunable parameters are introduced to the measurement matrix. Under white-light illumination, the scene will be significantly less sparse and the system will be severely underdetermined, requiring many more measurements for an accurate reconstruction of the data cube. This indicates that, depending on the level of sparsity in the light source, different measurement methods should be employed for accurate reconstruction. A simple way to match the measurements with the level of sparsity is to do multiframe capture. In some cases, a single snapshot will yield sufficiently accurate estimates; in other cases, a series of multiple frame captures with different encoding is necessary to optimize the measurement matrix and validate the sparsity constraint. This scalability in the measurements allows a single CASSI system to acquire data from virtually any scene.

C. Reconstruction Algorithm

CS stipulates that accurate and unique solutions to underdetermined systems can be found by solving sparsity-constrained optimization problems. Several

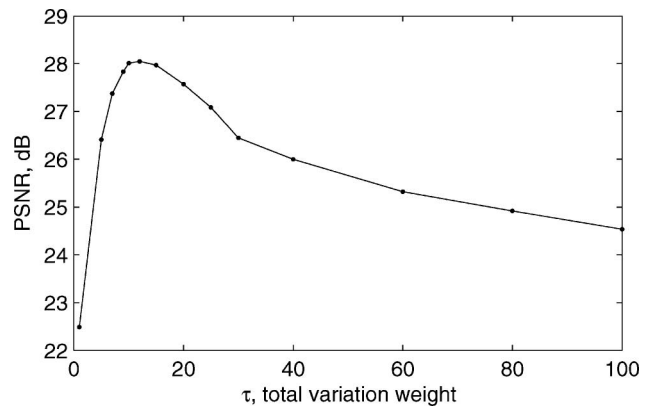


Fig. 1. τ versus PSNR for a ten-channel CASSI reconstruction using six frames and 100 iterations.

algorithms have been tested with the CASSI model, including gradient projection for sparse reconstruction (GPSR) [16,17], nested adaptive refinement estimation (NeARest) [6,18], sparse reconstruction by separable approximation (SpARSA) [19], and two-step iterative shrinkage/thresholding (TwIST) [17,20]. In general, TwIST has produced the most accurate and visually pleasing reconstructions while being an efficient algorithm that solves the Lagrangian unconstrained formulation of constrained optimization problems:

$$\hat{f}_{\text{TwIST}}(\tau, \Gamma) = \arg \min_f \left[\frac{1}{2} \|g - \Phi f\|_2^2 + \tau \Gamma(f) \right]. \quad (10)$$

The total variation (TV) regularizer, $\Gamma(f)$, is isotropic with a general 2D definition in Eq. (11), where Δ_h^f is the horizontal difference operator and Δ_v^f is the vertical difference operator. In Eq. (12), the difference operators are written explicitly, and, with a 3D data cube, the sum in k must be added as well:

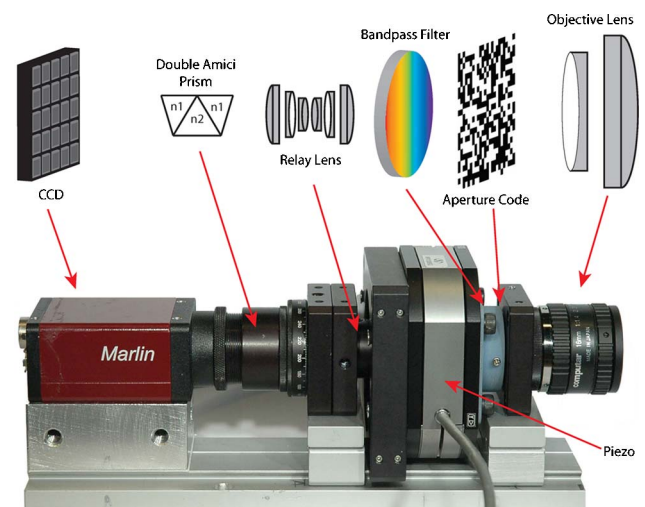


Fig. 2. (Color online) Schematic and photo showing the entire CASSI instrument. Left to right: CCD, double Amici prism, relay lens, piezo stage, bandpass filter, aperture code, and objective lens.

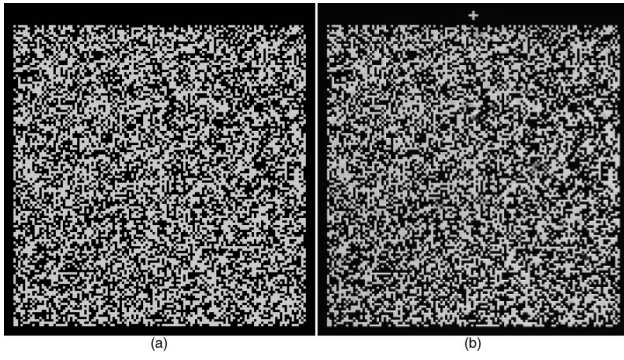


Fig. 3. (a) Ideal aperture code and (b) image of aperture code at detector under 550 nm monochromatic light. Notice the blur added to the aperture code relative to the ideal code.

$$\Gamma_{iTV}(f) = \sum_i \sqrt{(\Delta_i^h f)^2 + (\Delta_i^v f)^2}, \quad (11)$$

$$\begin{aligned} \Gamma_{TV}(f) \\ = \sum_k \sum_{i,j} \sqrt{(f(i+1,j,k) - f(i,j,k))^2 + (f(i,j+1,k) - f(i,j,k))^2}. \end{aligned} \quad (12)$$

The TV constraints are applied to each spectral slice independently, allowing steep gradient changes along the spectral axis. A tuning parameter τ in Eq. (10) specifies the relative weight of the constraints versus the data fidelity term. Figure 1 shows the relative peak signal-to-noise ratio (PSNR) values for different weights (τ) on the regularization term for a simulated CASSI system with multiple frames. From Fig. 1, it is evident that choosing too low a value of τ has severe consequences on the PSNR, while choosing too high a value is generally more stable.

3. Experimental Setup

The physical CASSI system in Fig. 2 was changed from the original system [6] by increasing the mag-

Table 1. PSNR versus Number of CASSI Frames for a Simulated CASSI Reconstruction on HYDIC Data Set

Frames	PSNR
1	21.3
4	24.5
12	28.6
16	27.4
24	30.1
32	30.5

nification of the aperture code on the detector from two pixels to three pixels, which altered the total dispersion from 33 to 53 pixels, increasing the number of spectral channels.

The aperture code is a random binary pattern, generated at one-half the resolution of the final mask and resampled using nearest interpolation so that each feature is at least two-by-two features. The mask is then magnified optically so that each two-by-two feature maps to a minimum of three-by-three pixels on the detector. Ideally, smaller mask features yield better resolution both spectrally and spatially, but diffraction and optical blur negate the advantages for smaller features and three pixels is a good compromise. Using translations at subfeature resolution (on the level of one pixel) achieves some super-resolution results, offsetting the larger feature sizes.

Calibration for the measurement matrix is done by imaging the aperture code at discrete wavelengths over the entire spectral range of the instrument. This accounts for the system point spread function, which includes blur and subpixel misalignment errors. The image of the aperture code at the detector under monochromatic light is shown in Fig. 3(b), while the ideal code is shown in Fig. 3(a).

The random mask pattern was chosen for several reasons: (1) the light throughput needs to be as constant as possible across the scene; (2) the columns in the mask should ideally be independent, which, for a

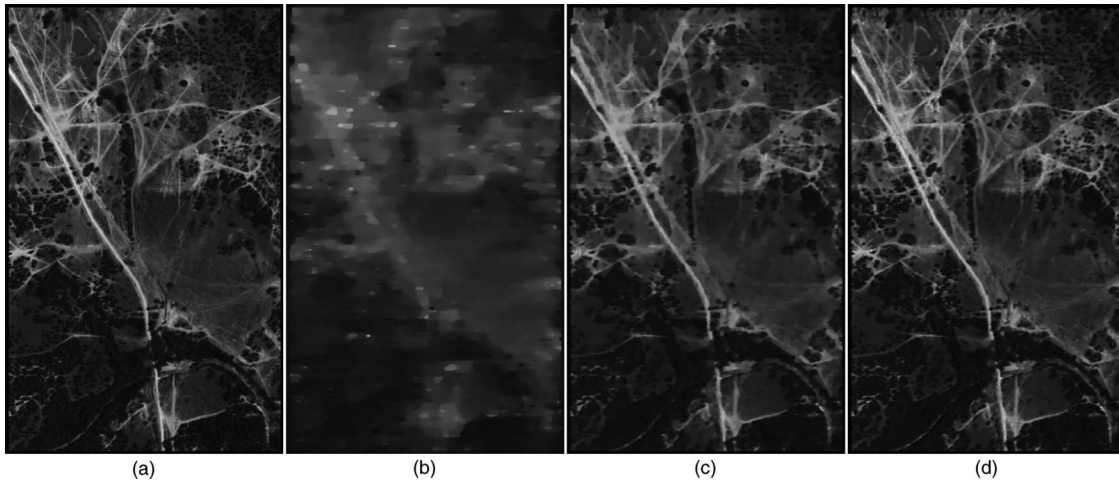


Fig. 4. Simulation using HYDICE data set for comparison of snapshot versus multiframe acquisition in a 41-channel sunlight illuminated scene. (a) Original image, (b) snapshot, (c) 12 frames, and (d) 32 frames.

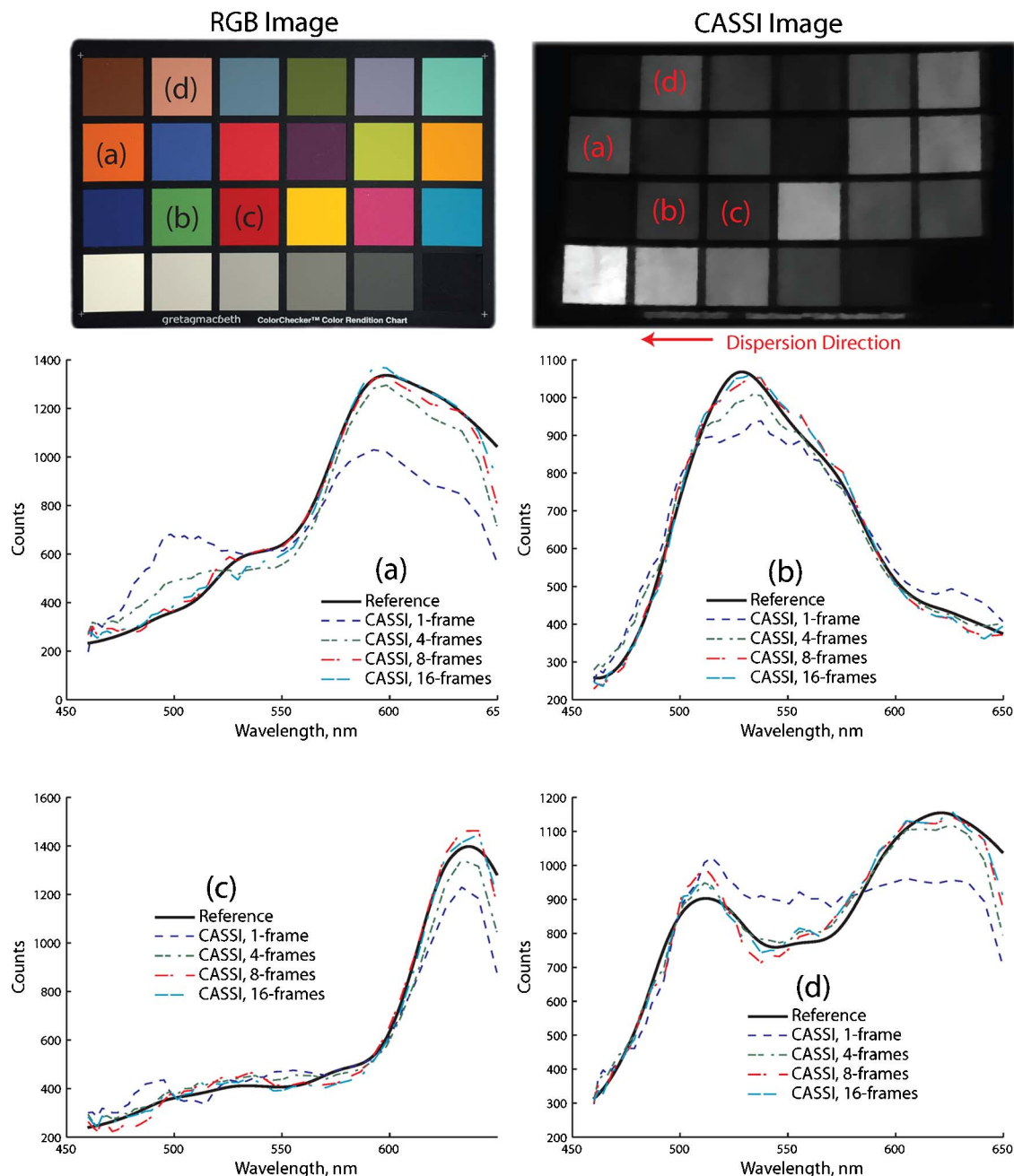


Fig. 5. (Color online) Using the GretagMacbeth ColorChecker as a baseline, comparisons were made with white-light sunlight emulation. (a)–(d) compare snapshot versus 4, 8, and 16 frame reconstructions. Nearby colors can bleed into the spectra, as seen in the RGB image, where the blue just to the right of the orange square was dispersed into the orange. Multiple frames eliminate this problem.

random mask, is not true, but over the span of dispersion generally holds; (3) compressive sensing prefers random codes.

Multiple snapshots g_i require distinct coding. Since physically replacing the mask with a different mask during capture is too slow, the mask was attached to a piezo system (Newport Corporation) that translates it by up to 24 pixels on the detector with a repeatability of 0.0068 pixel. Moving by three pixels, or equivalently one mask feature on the detector, yields a new code modulation corresponding to about $19.8 \mu\text{m}$ of linear translation. The piezo system is

mounted directly to the aluminum base of the CASSI system, so the only moving part is the piezo head, which has the absolute position recorded on the

Table 2. RMSE of CASSI Spectra versus Reference Spectrometer

Frames	Center				Edge			
	(a)	(b)	(c)	(d)	(a)	(b)	(c)	(d)
1	9.6%	6.9%	4.1%	17.4%	14.0%	11.7%	8.4%	34.3%
4	2.7%	3.6%	2.4%	4.5%	5.3%	8.1%	2.7%	10.2%
8	3.7%	3.3%	2.6%	5.4%	2.7%	3.6%	2.3%	8.9%
16	1.9%	3.4%	2.8%	5.0%	2.9%	4.1%	2.7%	6.8%

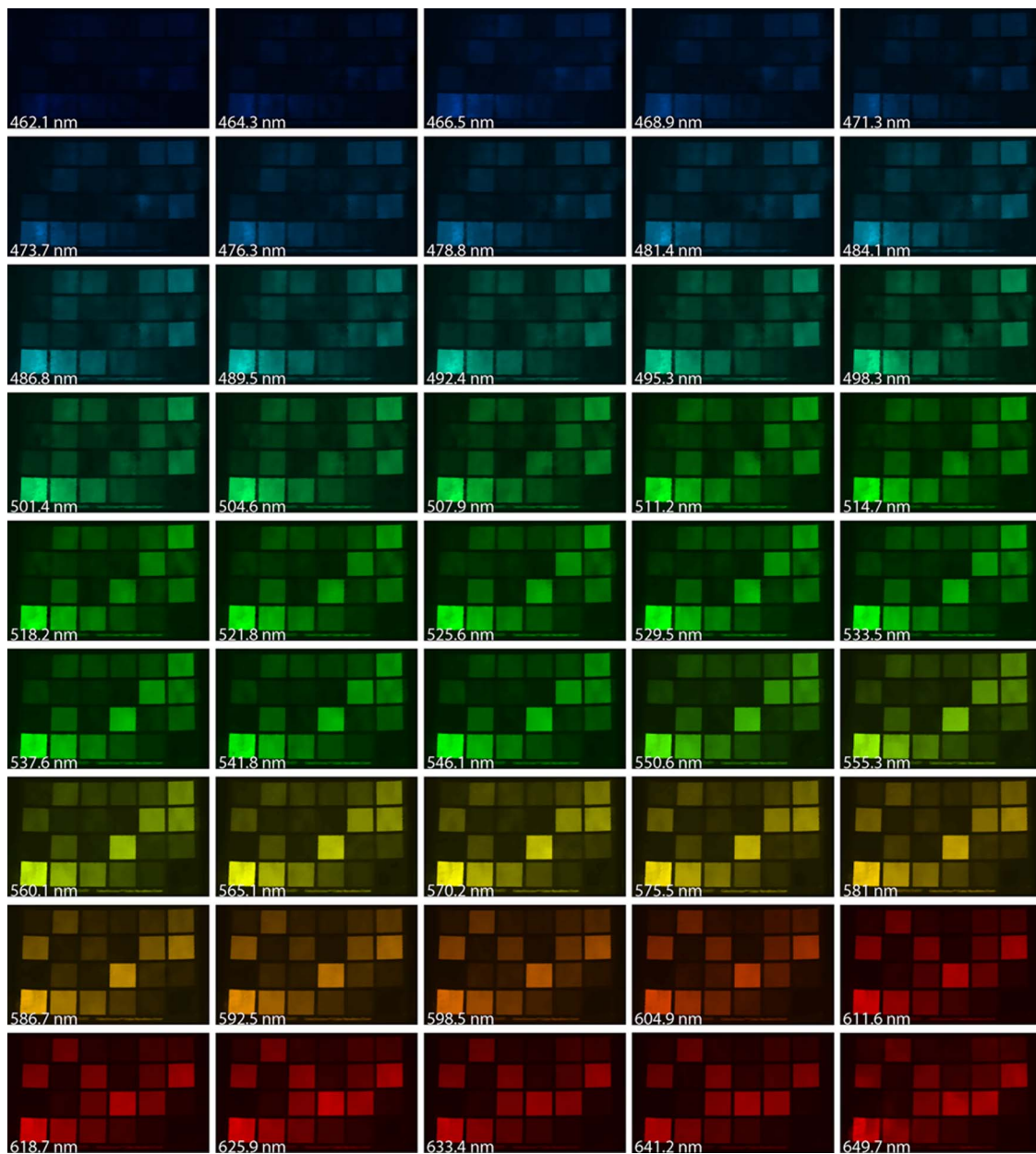


Fig. 6. (Color online) Multiframe CASSI reconstruction of the GretagMacbeth ColorChecker, showing all the channels from 460–650 nm.

controller. Any motion that does occur can be easily accounted for by an offset in software. A monochromatic source illuminating the aperture code is recorded before acquiring data, which can be compared to the calibration for any mask motion. In general, the piezo has not compromised system stability, so long as the controller has been turned on for at least 1 h to stabilize.

Control of the piezo system was entirely automated through a serial interface to MATLAB, enabling multiple frame captures with a single button click and storing the data to a single file, which can be read by a reconstruction GUI in MATLAB. Multiframe capture time varies depending on the exposure time and acquisition type. Currently, the system operates in two modes: (1) each image is

captured statically, after the mask has moved and is stable, with no limit on integration time; (2) the camera is constantly acquiring frames at 60 fps and the mask is constantly moving in a set pattern, slow enough to virtually eliminate motion blur. The first method is best for dark scenes that require long integration times, since the second method requires enough light for fast integration times.

The piezo takes 16 ms to move two pixels on the detector and 30 ms to move the entire range of 24 pixels. Typical integration times are between 10 and 50 ms, giving a frame rate of 12–38 fps in multiframe mode. In practice, it takes about 0.5 s to acquire 20 frames. If the piezo stops for each integration, the piezo needs 30 ms to stabilize plus 50 ms of integration time, dropping the frame rate

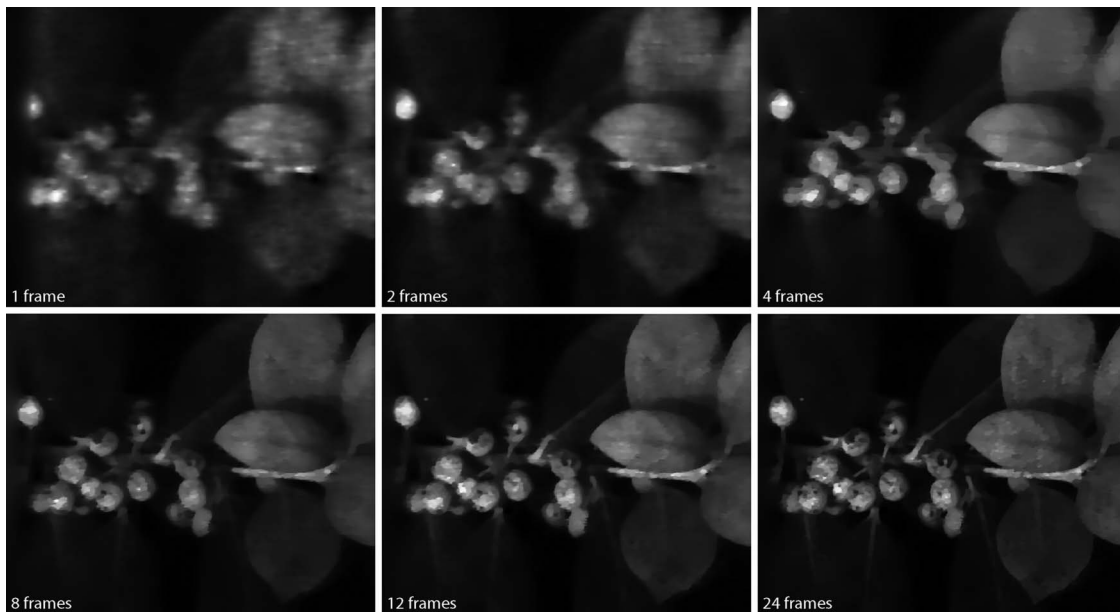


Fig. 7. Comparison between a single snapshot and various multiframe reconstructions for a single channel at 605 nm.

to 12.5 fps. If 24 frames are then required, a multi-frame sequence would take around 2 s, keeping in mind that each frame is a valid snapshot that can be fully reconstructed, while each additional frame adds to the measurement accuracy.

Reconstruction time using a dual-core system and a $256 \times 256 \times 21$ data cube, the snapshot takes about 80 s, a ten-frame reconstruction takes 113 s, and a 20-frame reconstruction takes 173 s, giving roughly a 2 times increase for 20 frames. For larger data sets, the ratio for 20 frames to snapshot drops down to 1.8. Using a multicore system, up to 16 frame reconstructions take no additional time; 64 frame reconstructions take roughly 2 times longer than a snapshot.

Specific to the algorithm, the measurement matrix H was implemented in functional form rather than matrix form due to its enormous size. All calculations were performed using single precision to reduce computational time and memory requirements; with no loss in quality from using double precision.

4. Experimental Results

Isolating the spatial resolution from the spectral resolution can be done through the use of bandpass filters, but this only tests the performance of the algorithm in restoring missing information from the coded aperture since there is no longer spectral

compression. Therefore, it is most instructive to investigate reconstructions in the general sense without attempting to isolate spatial and spectral resolution.

Using hyperspectral data from the HYDICE [21] sensor system, a simulation was run using an actual calibration cube from the CASSI system and 41 spectral channels. Multiframing data was simulated by running 41 channels of the HYDICE spectral image through the forward model in Eq. (8), where Φ_1 equals the calibration cube and Φ_N equals the calibration cube shifted according to the mask shifted by the piezo. The input g was then solved using the algorithm described in Eq. (10), with equal weighting τ for all six simulations. PSNR was then calculated for Table 1 by directly comparing the original HYDICE image to the output from TwIST. The PSNR will continue to increase for more frames, even if the system is no longer underdetermined because of increased signal-to-noise ratio in the algorithm. The slight drop in PSNR for 16 frames is because the weighting factor τ actually needs to be slightly higher for more frames because the nonideal aperture code does not completely overlap when shifted. Figure 4 shows the results of the simulation for channel 35 of the reconstructed data cube.

For the first example in Fig. 5, the GretagMacbeth ColorChecker was used. Parameters for the reconstruction were $\tau = 0.2$, 100 iterations, and 1, 4, 8, and 16 frames. The reference spectrum shown as the black curve was taken using an Ocean Optics USB2000 spectrometer. Note that, in all cases, the snapshot reconstruction correctly identifies the spectra, but if nearby colors are too close, they will bleed into the reconstruction. This can be seen for the RGB image, where the blue square is prior to the orange square along the line of dispersion, so if the channels are not separated adequately, some

Table 3. PSNR versus Number of CASSI Frames for Actual Data, Referenced to a 24-Frame Image in Fig. 7

Frames	PSNR
1	23.2
2	27.3
4	29.0
8	30.7
12	35.7

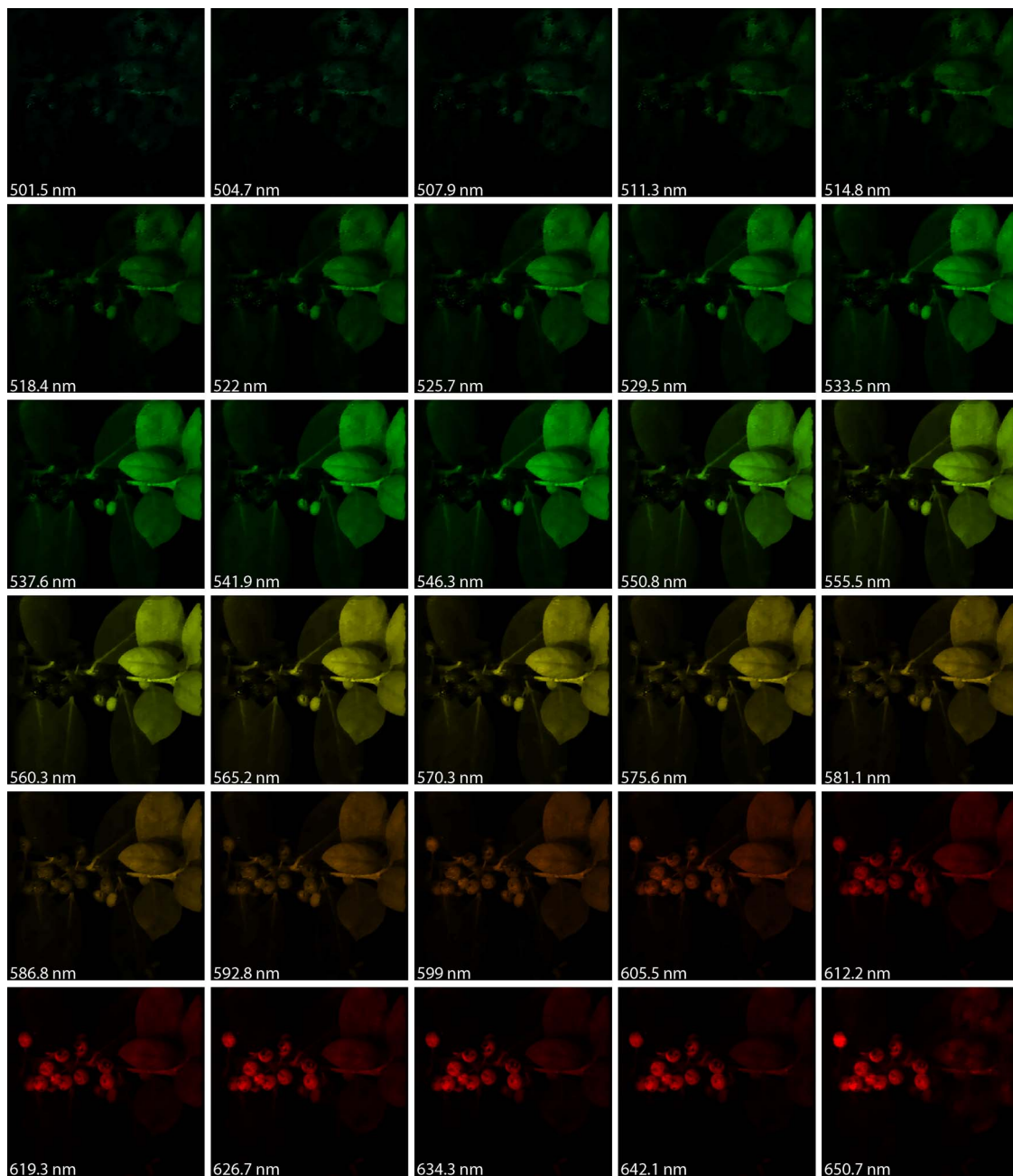


Fig. 8. (Color online) All channels from 500–650 nm from a 24-frame reconstruction of the data cube.

residual power from the blue remains in the orange channels. When eight or more frames are used, this problem is virtually eliminated. Thirty-two and 64 frames were also reconstructed, but the results showed marginal improvements for this target. The black edges around the squares are reconstructed as straight lines near zero with some offset depending on the spectral calibration.

Quantification of the spectral accuracy is summarized in Table 2, where each selected pixel's spectra is compared to the Ocean Optics spectra by normalized root mean square error. This comparison was done at both the center of the square and at the left edge.

Near the center, the spatial resolution is near uniform, but near the edge, multiframe reconstructions show significant improvements in the range of 5%–30%.

The reconstructed spectral information must be calibrated to correct for the nonuniform signal strength resulting from both the detector quantum efficiency and nonuniform spectral channel widths. Both of these errors are known and can be applied by weighting each channel after reconstruction, but, generally, a blind weighting yields poor results, especially when adding gain to a low signal. Alternatively, we have gotten better results from using the



Fig. 9. (Color online) RGB image of the holly leaf from a Nikon digital SLR.

reference spectra of a white object and applying this to the CASSI spectra of the white object, which can then be used to correct the entire data cube.

Figure 6 shows all the channels from the system, calibrated using the white reference spectra of the Ocean Optics taken from the ColorChecker white square at the bottom left of the RGB image in Fig. 5. This data cube was used to produce the spectra in Fig. 5 by selecting certain pixels and plotting out along the spectral dimension.

The second example in Fig. 7 uses a holly leaf to compare spatial and spectral resolution. Referring to the RGB image in Fig. 9, the berries are dark red, while the leaves are green. The same data was reconstructed using different numbers of frames, from a single snapshot to 24 frames. In this case, the quality will keep increasing even up to 64 or 128 frames because it is impossible to move the random mask and achieve independent measurements, regardless of the type of translation or rotation. Table 3 quantifies the differences between each image and the 24-frame reference.

The last example in Fig. 8 shows the same reconstruction, but with each channel explicitly shown from 500–650 nm. This reconstruction used 24 frames for the data cube estimation. The channels have been truncated since there is no signal below 500 nm.

5. Conclusion

Compressive spectral imaging has the advantage of very fast data cube acquisition, but if the scene is not highly compressible, the reconstructions exhibit reduced resolution. In this paper, we have proposed a highly adaptive system that will perform well in virtually any situation without sacrificing the ability to capture snapshot data at a full 30 fps. If the scene is static during a longer period of time, additional measurements can be used to refine the data cube, but if the scene is highly time dependent, each snapshot can still be used to estimate the data cube.

Comparisons were made between snapshot and multiframe reconstructions. Depending on the scene and spatial diversity, a single snapshot can accurately estimate the scene, but if additional information is needed, the same data set can be used to reconstruct high-resolution images. However, it is important not to compare snapshot systems to non-compressive methods and expect similar results. The value of the proposed system is that it can take both into account, in the same acquisition.

This work was supported by the U.S. Air Force Office of Scientific Research (USAFOSR).

References

1. D. J. Brady, *Optical Imaging and Spectroscopy* (Wiley-Interscience, 2008), pp. 387–390.
2. M. E. Gehm, S. T. McCain, N. P. Pitsianis, D. J. Brady, P. Potuluri, and M. E. Sullivan, “Static two-dimensional aperture coding for multimodal, multiplex spectroscopy,” *Appl. Opt.* **45**, 2965–2974 (2006).
3. S. T. McCain, M. E. Gehm, Y. Wang, N. P. Pitsianis, and D. J. Brady, “Coded aperture Raman spectroscopy for quantitative measurements of ethanol in a tissue phantom,” *Appl. Spectrosc.* **60**, 663–671 (2006).
4. M. E. Gehm, M. S. Kim, C. Fernandez, and D. J. Brady, “High-throughput, multiplexed pushbroom hyperspectral microscopy,” *Opt. Express* **16**, 11032–11043 (2008).
5. A. Wagadarikar, R. J., R. Willett, and D. J. Brady, “Single disperser design for coded aperture snapshot spectral imaging,” *Appl. Opt.* **47**, B44–B51 (2008).
6. A. A. Wagadarikar, N. P. Pitsianis, X. Sun, and D. J. Brady, “Video rate spectral imaging using a coded aperture snapshot spectral imager,” *Opt. Express* **17**, 6368–6388 (2009).
7. C. F. Cull, K. Choi, D. J. Brady, and T. Oliver, “Identification of fluorescent beads using a coded aperture snapshot spectral imager,” *Appl. Opt.* **49**, B59–B70 (2010).
8. B. K. Ford, C. E. Volin, S. M. Murphy, R. M. Lynch, and M. R. Descour, “Computed tomography-based spectral imaging for fluorescence microscopy,” *Biophys. J.* **80**, 986–993 (2001).
9. B. Ford, M. Descour, and R. Lynch, “Large-image-format computed tomography imaging spectrometer for fluorescence microscopy,” *Opt. Express* **9**, 444–453 (2001).
10. M. H. W. Johnson, D. W. W. Fink, and G. Bearman, “Snapshot hyperspectral imaging in ophthalmology,” *J. Biomed. Opt.* **12**, 014036 (2007).
11. L. Gao, R. T. Kester, N. Hagen, and T. S. Tkaczyk, “Snapshot image mapping spectrometer (IMS) with high sampling density for hyperspectral microscopy,” *Opt. Express* **18**, 14330–14344 (2010).
12. A. Gorman, D. W. Fletcher-Holmes, and A. R. Harvey, “Generalization of the Lyot filter and its application to snapshot spectral imaging,” *Opt. Express* **18**, 5602–5608 (2010).
13. E. J. Candès, “Compressive sampling,” in *Proceedings of the International Congress of Mathematicians* (European Mathematical Society, 2006), pp. 1433–1452.
14. P. Ye, H. Arguello, and G. Arce, “Spectral aperture code design for multi-shot compressive spectral imaging,” in *Digital Holography and Three-Dimensional Imaging*, OSA Technical Digest (CD) (Optical Society of America, 2010), paper DWA6.
15. H. Arguello and G. R. Arce, “Code aperture design for band selectivity in spectral imaging using cassi system,” in *Proceedings of the European Signal Processing Conference (EUSIPCO)* (European Association for Signal Processing, 2010).
16. M. Figueiredo, R. Nowak, and S. Wright, “Gradient projection for sparse reconstruction: application to compressed sensing

- and other inverse problems,” *IEEE J. Sel. Top. Signal Process.* **1**, 586–597 (2007).
17. A. A. Wagadarikar, N. P. Pitsianis, X. Sun, and D. J. Brady, “Spectral image estimation for coded aperture snapshot spectral imagers,” *Proc. SPIE* **7076**, 707602 (2008).
 18. X. Sun and N. P. Pitsianis, “Solving non-negative linear inverse problems with the NeAREst method,” *Proc. SPIE* **7074**, 707402 (2008).
 19. S. Wright, R. Nowak, and M. Figueiredo, “Sparse reconstruction by separable approximation,” *IEEE Trans. Signal Process.* **57**, 2479–2493 (2009).
 20. J. Bioucas-Dias and M. Figueiredo, “A new twist: two-step iterative shrinkage/thresholding for image restoration,” *IEEE Trans. Image Process.* **16**, 2992–3004 (2007).
 21. P. A. Mitchell, “Hyperspectral digital imagery collection experiment (HYDICE),” *Proc. SPIE* **2587**, 70–95 (1995).